The bone ecosystem facilitates multiple myeloma relapse and the evolution of heterogeneous proteasome inhibitor resistant disease.

Authors/affiliations

Anna K. Miller[1]*, Ryan T. Bishop[2]*, Tao Li[2], Kenneth H. Shain[2,3], Niveditha Nerlakanti[2,4], Conor C. Lynch[2]+, David Basanta[1]+

Departments of [1]Integrated Mathematical Oncology, [2]Tumor Biology and [3]Malignant Hematology, H. Lee Moffitt Cancer Center and Research Institute, Tampa, Florida and the [4]Cancer Biology Ph.D. Program, University of South Florida, Tampa, Florida, USA.

Abstract

Multiple myeloma (MM) is an osteolytic plasma cell malignancy that, despite being responsive to therapies such as proteasome inhibitors, frequently relapses. Understanding the mechanism and the niches where resistant disease evolves remains of major clinical importance. Cancer cell intrinsic mechanisms and bone ecosystem factors are known contributors to the evolution of resistant MM but the exact contribution of each is difficult to define with current *in vitro* and *in vivo* models. However, mathematical modeling can help address this gap in knowledge. Here, we describe a novel biology-driven hybrid agent-based model that incorporates key cellular species of the bone ecosystem that control normal bone remodeling and, in MM, yields a protective environment under therapy. Critically, the spatiotemporal nature of the model captures two key features: normal bone homeostasis and how MM interacts with the bone ecosystem to induce bone destruction. We next used the model to examine how the bone ecosystem contributes to the evolutionary dynamics of resistant MM under control and proteasome inhibitor treatment. Our data demonstrates that resistant disease cannot develop without MM intrinsic mechanisms. However, protection from the bone microenvironment dramatically increases the likelihood of developing intrinsic resistance and subsequent relapse. The spatial nature of the model also reveals how the bone ecosystem provides a protective niche for drug sensitive MM cells under treatment, consequently leading to the emergence of a heterogenous and drug resistant disease. In conclusion, our data demonstrates a significant role for the bone ecosystem in MM survival and resistance, and suggests that early intervention with bone ecosystem targeting therapies may prevent the emergence of heterogeneous drug resistant MM.

Introduction

Multiple myeloma (MM) is the second most common hematological malignancy in the US[1], characterized by the clonal expansion of plasma cells localized primarily in the bone marrow microenvironment of the skeleton. In the bone microenvironment, MM cells disrupt the finely tuned balance of trabecular and cortical bone remodeling to generate osteolytic lesions. This is primarily via MM-induced inhibition of osteoblastic bone formation and increase of osteoclastic bone resorption. There are currently several approved therapies to treat MM including, but not limited to, proteasome inhibitors (e.g., bortezomib and carfilzomib), chemotherapy (e.g., melphalan), immunomodulatory drugs (e.g., lenalidomide), and cellular and non-cellular immunotherapies (e.g., BCMA CAR-T cells and daratumumab) that significantly contribute to the long-term survival of MM patients[2]. However, MM remains fatal as nearly all patients ultimately become refractory to various lines of therapy. A greater understanding of how resistant MM emerges in the clinical setting can yield new treatment strategies to slow relapse times and extend the efficacy of standard of care therapies.

In MM and other cancers, the tumor microenvironment is a well-known contributor to the development of treatment resistance. MM is an archetype of cancer cell-stroma interactions whereby MM cells reside and metastasize systemically within the bone marrow microenvironment[3]. In the bone ecosystem, MM interacts closely with mesenchymal stem cells (MSCs) and other progenitor cells[4-8] that secrete MM pro-survival and proliferative factors. Additional studies have shown that the bone marrow microenvironment can also protect MM cells from applied therapy in a phenomenon known as environment mediated drug resistance (EMDR)[9-11]. Reciprocally, it is well established that MM-derived factors stimulate osteoblast lineage cells to recruit and activate osteoclasts through RANKL production, which in turn degrade the bone matrix to release stored cytokines and growth factors (e.g., TGF-β) that support MM survival and growth. MM cells also suppress osteoblast maturation, thus tipping the balance towards excessive bone destruction. This vicious cycle leads to complications for MM patients such as hypercalcemia and pathological fracture that greatly contribute to morbidity and mortality[12].

While EMDR can contribute to drug resistance, MM intrinsic mechanisms, such as genetic and epigenetic alterations, also play a significant role in the process. For example, increased expression of the anti-apoptotic BCL2 protein family is important in mediating MM resistance to proteasome inhibition[13-16]. In fact, depending on selective pressures by different lines of therapies and clonal mutation capacity, MM may evolve to develop multiple mechanisms of resistance. While EMDR and intrinsic drug resistance mechanisms contribute to the emergence of refractory disease several questions remain: 1) How does the interplay between each mechanism contribute to the evolution of resistant MM? 2) How does each mechanism contribute to the heterogeneity of the disease under either control or treatment conditions? 3) Could targeting EMDR alter the course of the disease or its responsiveness to applied therapy thereby yielding significantly greater depths of treatment response? In the context of the bone marrow microenvironment and the direct/indirect communications occurring in a temporal and spatial fashion between MM and stromal cells, these questions remain difficult to address using current *in vivo* and *ex vivo* approaches.

Mathematical models of the tumor microenvironment, especially hybrid cellular automata (HCA) models (spatial models that couple discrete cell-based models with partial differential equations), have become a valuable approach that allows us to interrogate the interactions between multiple cellular populations over time under normal or disease conditions. Further, mathematical models have the potential for clinical translatability and can be used to study the impact of treatment on the tumor microenvironment and delay the onset of resistant disease[17-24]. We therefore leveraged these modeling approaches to examine MM progression and spatial evolution in response to therapy. To this end, we generated a novel HCA model powered by biological parameters from a mouse model of MM and demonstrate how it captures both normal bone turnover, and spatiotemporal cellular dynamics during MM progression in bone, such as loss of osteoblasts, increased stromal cell infiltration, osteoclast formation, and osteolysis. Additionally, we incorporate the proliferative and protective bone marrow microenvironment effects on MM mediated by osteoclastic bone resorption and bone marrow stromal cells. In the treatment setting, the HCA demonstrates that EMDR contributes to minimal residual disease, protecting tumors from complete eradication.

Moreover, this reservoir of MM cells increases the likelihood of unique resistance mutations arising over time and greatly contributes to the evolution of MM heterogeneity over time compared to non-EMDR scenarios. These results highlight the importance of the bone marrow microenvironment in contributing to MM resistance and patient relapse and provide a strong rationale for targeting both the MM and bone marrow microenvironment mechanisms for optimal treatment response.

Results

The HCA model recapitulates the key steps of trabecular bone remodeling

Trabecular bone remodeling is a continuously occurring process that is essential for regulating calcium homeostasis and bone injury repair such as microfractures (Fig. 1a) [25,26]. This process occurs asynchronously throughout the skeleton at individual sites known as basic multicellular units (BMUs). The BMU in our HCA consists of five different cell types, including precursor osteoclasts (pOCs), active osteoclasts (aOCs), mesenchymal stem cells (MSCs), precursor osteoblasts (pOBs), and active osteoblasts (aOBs). Additionally, we include central signaling molecules such as RANKL, a driver of pOC motility and OC formation and osteoclastic release of bone derived factors (BDFs) such as transforming growth factor beta of which bone is a major reservoir[27]. In the HCA, we use TGF-β as a representative BDF for its ability to modulate pOB proliferation and maturation to bone forming aOBs. We defined the roles and interactions of these key cellular populations and the factors that govern their behavior during the remodeling process using parameters derived experimentally or from the literature (Fig. 1b-c and Supplementary Tables 1-6). It is important to note that each cell in the HCA behaves as an autonomous agent that can respond to surrounding environmental cues independently. In our HCA model, new bone remodeling events are initiated over time at randomly selected locations such that multiple BMUs may be present at a given time. We demonstrated that each BMU undergoes five key phases of bone remodeling: initiation, resorption, reversal, formation, and quiescence[28] ultimately returning to homeostasis (Fig. 2 and Supplementary Video 1). We also observed that each simulation (n = 25) generated multiple BMUs over time, resulting in the replacement of the majority of the bone over a

four-year period (Fig. 2, Supplementary Video 1, Supplementary Fig. 1). We also noted that while the bone area to total area (BA/TA) remains relatively constant the shape of the trabecular bone changes, underscoring the dynamic nature of HCA model and how it reflects the *in vivo* scenario.

The HCA model captures dose-dependent effects of BDF and RANKL

To challenge the robustness of our bone remodeling HCA, we altered the levels of key factors controlling bone homeostasis. Our *in vitro* experimental data show that neutralizing TGF-β or addition of exogenous TGF-β in osteoblastic cell cultures increases and decreases mineralization respectively, a finding that is consistent with the literature[27,29,30] (Supplementary Fig. 2a). Similarly, lowering TGF-β levels *in silico* led to a dramatic increase in bone volume (Supplementary Fig. 2b-e). Interestingly, the HCA results showed that when TGF-β levels dropped below 90%, there was significant bone loss (Supplementary Fig. 2b-e) due to abrogation of MSC proliferation leading to reduced numbers of preosteoblasts that could contribute to bone formation (Supplementary Fig. 2e). These data are reflective of the known biphasic roles of TGF-β on cell behaviors and processes at high and low concentrations[27,29,30]. In addition, we demonstrated the sensitivity of OC formation in the HCA model in response to changes in RANKL levels (Supplementary Fig. 2f-h).

The HCA model integrates the impact of standard of care therapies on bone remodeling

Next, we assessed the response of the HCA model to standard of care therapies used for the treatment of MM such as zoledronate (ZOL) and bortezomib (BTZ). These compounds can block osteoclast function and formation respectively but, as we and others have shown, they can also stimulate osteoblast mediated bone formation[31-34] (Supplementary Fig. 3a-b and Supplementary Fig. 4a-b). Our results show that, as expected, both zoledronate (ZOL) and bortezomib (BTZ) therapy increased bone volume over the treatment period by enhancing osteoblastic bone formation and blocking osteoclast activity/formation (Supplementary Fig. 3c-h, Supplementary Fig. 4c-h). While OCs are impacted by both treatments, the HCA recapitulates their distinct mechanisms

of action showing that ZOL targets actively resorbing osteoclasts as demonstrated by a reduction in bone resorption per OC (Supplementary Fig. 4h) while BTZ limits the fusion of OC precursors as shown by a reduction in cumulative osteoclast numbers with treatment (Supplementary Fig. 3g). Collectively, these data demonstrate the ability of our HCA model to capture normal bone remodeling over extended periods and the appropriate response of the model to applied therapeutics.

The HCA model incorporates the MM-bone ecosystem vicious cycle

A key component of MM growth involves the initiation of a feed-forward vicious cycle leading to reduced bone formation and enhanced osteoclastic bone destruction (Fig. 1a). MM is also known to interact with several cellular components of the bone ecosystem such as MSCs in response to secreted growth factors and cytokines[11,35]. To incorporate these effects and MM growth characteristics into the HCA, mice were inoculated with U266-GFP MM cells and at end point, bones were processed and stained for proliferation (Histone H3 phosphorylation (pHH3)) and apoptosis markers (Terminal deoxynucleotidyl transferase dUTP nick end labeling (TUNEL)). Our data show that the highest proportion of proliferating MM cells are located within 50μm of bone (Fig. 3a-b) while fewer cells (TUNEL+) underwent apoptosis in this area (Fig. 3c-d) highlighting the protective effect of BDFs being generated from bone degradation. To consider the effect of bone marrow stromal cells on MM cells distal from bone, we performed *in vitro* experiments and found a significant increase in the proliferation of MM cells grown in the presence of conditioned medium from MSCs and pOBs, but not aOBs (Fig. 3e-f). To integrate these observations into the HCA, we assume that the intrinsic rate of MM cell division increases with BDF and when a pOB or MSC is near the MM cells (Fig. 3g-h and Supplementary Equation 11).

Next, to study the interactions of the MM-bone marrow microenvironment in the HCA model, we initialized each simulation with a single MM cell near a newly initiated bone remodeling event and the formation of an aOC. This assumption is a simplification of the colonization process, in which rare colonizing myeloma cells migrate to the endosteal niche[36,37]. The HCA model revealed exciting temporal dynamics where MM promotes successive phases of bone destruction mediated by osteoclasts that in turn

drives MM growth, thereby successfully recapitulating the vicious cycle (Supplementary Fig. 4a and Supplementary Video 2). As expected, the mathematical model demonstrated increasing tumor burden over time (Fig. 4a-b) with rapid loss of bone, correlating inversely with tumor burden (Fig. 4c-d). These findings are consistent with *in vivo* data obtained from the U266-GFP mouse model of MM which showed increasing levels of GFP positive cells in the bone marrow following *ex vivo* flow cytometric analysis (Fig. 4e), with rapid onset of trabecular bone loss (BV/TV; Fig. 4f-g) and associated trabecular bone parameters as assessed by high resolution μCT (Supplementary Fig. 5). The similarities in trends between the *in vivo* model and the HCA outputs, indicated that the HCA model was accurately recapitulating the MM-bone vicious cycle.

Furthermore, the spatial and temporal nature of the HCA allowed us to make several observations: 1) In the model, the recruitment of MSCs *in silico* increases over time (Fig 5a) as we and others have previously reported[38,39], 2) the model accurately shows a suppression of adult osteoblast formation (Fig. 5b) due to inhibition of differentiation by MM[35,40], and 3) the model predicts an early increase in pOBs followed by a reduction (Fig. 5c), consistent with previous reports[41], while there is a concomitant increase in osteoclasts (Fig. 5d) [35,40]. We also compared these population dynamics with our *in vivo* model. In tissue sections derived the U266-GFP model from various time points (days 10, 40 and 100), we measured MSC, pOB, OB, and OC content and observed strong agreement with cell population trends generated by the MM HCA (Fig. 5e-h and Supplementary Fig. 6). Taken together, these data demonstrate the ability of the MM HCA to capture the vicious cycle of MM progression in the bone microenvironment over time.

Environment-mediated drug resistance increases minimal residual disease and leads to higher relapse rates

We and others have shown that BTZ demonstrates a dose dependent cytotoxic effect on MM (Supplementary Fig. 3a)[42,43]. The compound is also effective *in vivo* but MM still grows albeit at a significantly slower rate. Patients also typically become refractory to BTZ. This indicates that MM cells are 1) protected by the surrounding bone ecosystem, or 2) due to selective pressure and mutation, drug resistant clones emerge, or 3) that both ecological and evolutionary contributions can occur in parallel. Here we sought to use

the spatial nature of the HCA model to gain a deeper understanding of how MM resistance evolves focusing initially on the contribution of bone ecosystem, i.e., EMDR. We confirmed the EMDR protective effect conferred by bone stromal cells on MM in the presence of BTZ *in vitro* (Fig. 6a) and integrated this effect into the HCA model (Fig. 6b). BDF was also included since it can provide a survival advantage to MM cells in the presence or absence of treatment[44,45]. Next, we initialized HCA simulations with a homogeneous sensitive MM population. BTZ was applied once the tumor burden reached a volume of 10% to mimic the scenario of diagnosis in the clinical setting. Our results show that without EMDR, BTZ completely eradicated the disease at high doses (Fig. 6d, Supplementary Fig. 3j), consistent with our *in vitro* findings. However, when EMDR effects are included in the model, BTZ reduced MM burden significantly, but the disease persisted at a stable, albeit lower, level and did not grow over time compared to existing *in vivo* data (Fig. 6c-d). These data suggest that EMDR does not directly contribute to MM relapse but does protect a small volume of MM cells from BTZ. Therefore, to address the relapse and the emergence of BTZ resistance in MM cells, we integrated a mutational probability ($p_{mut} = 10^{-4}$ or $p_{mut} = 10^{-3}$) during cell division, which allowed for the emergence of BTZ resistance. Based on our *in vitro* observations, we also incorporated a cost of resistance[46] in the model such that BTZ-resistant cells proliferate at a slower rate and are out-competed by PI-sensitive cells in the absence of treatment (Supplementary Fig. 7).

We then repeated our *in-silico* experiments and observed that with the lower mutation probability ($p_{mut} = 10^{-4}$), EMDR increased the likelihood of tumor progression with more simulations likely to relapse (54.4%, n = 125) compared to tumors without EMDR (6.4%, n = 125; Fig. 6e and g; Supplementary Video 3). Similarly, with a higher mutation probability ($p_{mut} = 10^{-3}$) tumors were more likely to relapse when EMDR is present (100%, n = 25) compared to tumors without EMDR (56%, n = 25, Fig. 6f and h; Supplementary Video 4). However, the higher mutation probability also increased the likelihood of tumor progression regardless of EMDR, implying a greater role for MM intrinsic resistance mechanisms during tumor relapse. To strengthen these findings, we tested a different treatment strategy, in which BTZ therapy was pulsed (2 weeks on, 1 week off) and observed similar results (Supplementary Fig. 8). Moreover, during BTZ application, EMDR protected a portion of sensitive cells (Fig. 7a-b; Supplementary Fig.

9a). This protected reservoir of sensitive MM cells ultimately develops intrinsic resistance leading to the increased relapse rates observed. The role of this sensitive reservoir in relapse is particularly evident at the lower mutation probability, where tumors with EMDR exhibited more variable (generally longer) relapse times compared to tumors without EMDR. When EMDR is absent, many tumors go extinct and relapse only occurs if intrinsic resistance arises early following treatment, whereas with EMDR, sensitive cells persist and resistance can arise later in the course of the disease. Taken together, these results demonstrate the ability of the HCA to predict the effect of mutation probability and EMDR on tumor relapse and indicate a vital role of EMDR in contributing to minimal residual disease and the development of relapse refractory MM.

Environment-mediated drug resistance and mutation probability impact heterogeneity in relapsed disease

Even though relapsed tumors with a high mutation probability had similar growth dynamics with and without EMDR, we noted that the composition of the tumors differed greatly. Myeloma is a clonal disease with the prevalence of clones changing throughout treatment[36,47-49]. Given the spatial resolution of the HCA model, we next asked whether EMDR impacted the heterogeneity of resistant tumors. To this end, we tracked the number and spatial localization of new clones forming from unique mutation events under BTZ treatment conditions in the presence or absence of EMDR. We observed that at a high mutation probability ($p_{mut} = 10^{-3}$) EMDR drove the evolution of significantly more resistant subclones (mean = 5.2 subclones with >10 cells, n = 24 simulations) compared to non-EMDR conditions where the arising population was composed largely of a single resistant clone (mean = 1.2 subclones with >10 cells, n = 10 simulations; Fig. 7c-d), with similar results at lower mutation probabilities and pulsed BTZ treatment (Supplementary Fig. 9b-c). Moreover, the HCA revealed a significant proportion of resistant subclones originated in close proximity to MSCs/pOBs (Fig. 7c) or following release of BDF from osteoclastic bone resorption (Supplementary Fig. 9c). Taken together, these data would indicate that EMDR not only leads to enhanced relapse, but increased MM heterogeneity due to the emergence of independent resistant MM clones. Further, it is also plausible that EMDR may give rise to MM clones with potentially unique intrinsic BTZ resistance

mechanisms making the treatment of relapsed tumors more challenging. Together, these data support that early targeting of bone marrow microenvironment, and thus EMDR, would lead to reduced MM heterogeneity and potentially deeper responses with subsequent lines of treatments.

Discussion

Understanding the factors that govern the evolution of refractory MM remains of huge clinical importance. Dissecting how intrinsic and bone ecosystem mechanisms contribute to the evolution of the disease in the presence or absence of treatment or where these clones arise spatially are difficult questions to address with standard experimental techniques alone. Here, we address this using a novel experimentally derived hybrid cellular automaton (HCA) model of MM evolution in the bone ecosystem that provides new insights. For example, we show that the bone ecosystem contributes to minimal residual disease, and MM clonal heterogeneity. These findings are in part supported by previous studies revealing enrichment of binding proteins and chemokine receptors on MM cells in minimal residual disease, indicating a likely role for stromal interactions in facilitating relapse[50]. Our findings and additional wider biological validation provide rationale for the targeting of the bone ecosystem during the application of standard of care treatment to prevent the emergence of multiple resistant clones.

Our own *in vitro* and *in vivo* data, as well as data from the literature, were used where possible to parameterize and calibrate the HCA model. However, there were some parameters that could not be estimated, and the specific assumptions that have been incorporated into the HCA may impact the generality of the results. For example, we assume that MSCs are recruited in proportion to tumor burden based on experimental data in non-treatment conditions, but the application of treatment could alter this recruitment rate and thus bone ecosystem protective effects. Furthermore, there are limitations to how well parameters estimated from *in vitro* data correspond to the *in vivo* setting. To address this, we tested the robustness of the model results by varying a subset of parameter values to determine the impact on simulation results (Supplementary Methods 1.4; Supplementary Fig. 10). Overall, our finding that EMDR increases minimal

residual disease and leads to higher relapse rates was consistent across parameter values, underscoring the robustness of the model.

There have been several mathematical models that explore interactions between MM and the bone marrow microenvironment. For example, ordinary differential equation (ODE), evolutionary game theory (EGT), and hybrid agent-based models have revealed insights into MM growth in bone and have even taken into consideration the impact of MM progression on bone destruction[51-57]. Additionally, mathematical models have focused on how ecosystem effects contribute to drug resistance[58-61]. Importantly, the HCA model presented herein represents a significant advance in that it is carefully integrated with biological data to recapitulate the bone-MM ecosystem under normal and treatment conditions and is the first model to dissect intrinsic vs. ecosystem driven resistance in multiple myeloma. A major additional advantage of our model is its spatial nature, allowing us to visualize and measure where the ecosystem, and particularly stromal cells, contribute to the generation of resistant clones.

Our model shows that resistant MM clones can arise independently of the bone ecosystem during BTZ treatment if the mutation probability is sufficiently high. But, when EMDR is present, we observe the evolution of higher numbers of resistant clones near MSCs/pOBs/BDF during continuous BTZ treatment. The model also suggests that targeting of EMDR during treatment would reduce MM heterogeneity. Various adhesion molecules and cytokines such as the CXCL12/CXCR4 and IL-6/JAK/STAT axis have been shown to mediate ecosystem protective effects and drugs/biologics that specifically target those pathways have been trialed[62,63]. Unfortunately, these drugs have had little success translating to clinical practice due to limited survival improvements when added to existing therapies[64]. However, we posit that early intervention with EMDR-targeting agents, perhaps in combination, would reduce tumor heterogeneity, rendering relapsing tumors vulnerable to a targeted second line therapy that targets the predominantly homogenous disease. As such, future studies/trials should take into consideration the tumor diversity upon relapse and response to second line therapies.

Another important aspect of the model is the ability to apply and withdraw therapy at varying stages of MM progression to quantitatively determine the impact on MM over time which may be useful for adaptive therapy design and implementation. Adaptive

therapy is an emerging, evolution-inspired approach for cancer treatment that exploits competitive interactions between drug sensitive and drug resistant cells to maintain a stable tumor burden[46]. Several models have studied the many ways therapies can be applied in an adaptive manner ensuring that the competition between treatment resistant and naïve populations allows for better overall survival for cancer patients. Importantly, our model captures tumor interactions with the bone ecosystem and thus includes the potential impact of the bone ecosystem on adaptive therapy. This allows us to study not only how treatments impact tumor populations but also their influence on bone ecosystem cells such as osteoblasts and osteoclasts, and how this can then influence MM response since the protective bone microenvironment can serve as a reservoir of sensitive cells under treatment. Clinical trials thus far using adaptive therapy guided by mathematical modeling have had encouraging results. For instance, recent studies have shown that in patients with bone metastatic prostate cancer, adaptive therapies guided by mathematical models can increase the time to progression and the overall survival using standard of care treatments[65]. These data support the feasibility of integrating mathematical modeling for the design of patient specific treatment. It should be noted however, the HCA model is parameterized with a variety of in vitro, in vivo, and human data, making translation directly to the clinic challenging in its current form. This can be resolved with further rigorous model calibration and validation using clinical data, and multiple efforts at moving agent-based models into the clinical setting are underway[22-24,66,67].

A key component of our HCA model lies in its ability to recapitulate the homeostatic nature of bone remodeling over prolonged periods (~4 years). As we demonstrated, the impact of therapies on tumor-naïve bone volume and the bone stromal cellular components that control the process can also be quantitatively examined. It also can examine non-cancerous bone diseases that result from an imbalance in bone remodeling such as osteoporosis[68]. The underlying causes of osteoporosis can result in differing effects on osteoclasts and osteoblasts, which could be incorporated into the model. For example, estrogen deficiency increases the lifespan of osteoclasts while having the opposite effect on osteoblasts, whereas age-related senescence is characterized by decreased osteoclastogenesis and osteoblastogenesis[68]. Osteoporosis treatments include anti-resorptive therapies (e.g., bisphosphonates) and bone formation therapies

(e.g. intermittent PTH). By modifying certain model parameters, we can explore the effect of different therapeutic strategies on disease outcomes to determine if certain treatments are more effective in particular scenarios[69]. Importantly, the temporal and cellular resolution of the model also can identify key moments in which to administer treatments to maintain a healthy bone volume.

Our HCA model, like all models, has caveats. For example, its two-dimensional nature does not take into account the potential three-dimensional role in evolutionary dynamics[70,71] or the vascular nature of the bone marrow-MM microenvironment that can play a role in drug/nutrient diffusion,[72,73]. However, these can be incorporated into the model if necessary, upon availability of relevant experimental data. Another potential and future extension of the model is to incorporate the immune ecosystem given its role in controlling bone turnover and cancer progression[72,73]and the growing armamentarium of immunotherapies in MM. Here, we excluded the immune component to focus solely on the role of the bone stroma on MM progression combined with the fact that MM growth in immunocompromised mice was used to parameterize and compare model outputs. Infiltrating immune cells have noted effects on cancer progression. For example, initially, natural killer (NK) cells and cytotoxic T lymphocytes can drive an anti-tumor response[74]. However, as the tumor progresses, immunosuppressive populations expand including myeloid derived suppressor cells (MDSCs) and regulatory T-cells (Tregs)[74]. MM is characterized by an increase of inactive NK cells, MDSCs, and Tregs and treatments such as bortezomib can alter the composition and activity of infiltrating or resident immune cells[74,75]. Tumor-immune dynamics in MM have been previously explored with ODE models[76,77] and parameters derived from *in vitro* or *in vivo* studies can be integrated into our HCA model albeit with a limit on complexity. Another caveat is the difficulty in determining the rate of MM mutation and the assumption that it occurs intrinsically due to treatment pressure. Prior studies suggest that drug resistance may arise through the selective expansion of pre-existent resistant tumor cells, *de novo*, or through the gradual increase in resistance over time[78]. In our model, we assume that after treatment initiates (i.e. once the bone marrow consists of 10% of MM cells), there is a probability that a dividing MM cell could mutate, and that mutation directly causes resistance to bortezomib resulting in heterogeneity. This mutation probability that would lead to treatment

resistance is difficult to assess in patients or in experimental models but the resultant heterogeneity arising from different mutation probabilities may allow us to infer mutation rates in patients. Although we have focused on intrinsic resistance in the current study, it is also possible to seed the model with various clones that have differing traits/resistance and conduct simulations to examine the subsequent impact on MM evolution.

In conclusion, we have described a new mathematical model of MM evolution in the context of the bone ecosystem. Our results show that, under treatment conditions, the interactions between the bone ecosystem and the tumor contributes to the presence of residual disease and to the enrichment of tumor heterogeneity. These results suggest that early intervention with drugs that target the bone ecosystem could lead to MM extinction or at the very least reduce tumor heterogeneity by preventing the evolution of multiple drug resistant clones. Given the current interest in novel strategies of treatment that consider the evolutionary dynamics in cancer such as adaptative therapies, we also predict that our model can be a useful clinical tool in guiding patient specific treatment strategies.

Methods

Hybrid Cellular Automaton Model

The model we developed builds on the HCA paradigm first described by Anderson *et al.* and used to study evolutionary dynamics in cancer and our work in the context of bone metastasis[79-83]. By definition, an HCA consists of discrete cell types that are updated once per time step according to a set of flow charts (Fig. 1c) as well as a set of partial differential equations that describe cytokines in the microenvironment. Here, we consider six different cell types, including precursor osteoclasts (pOCs), active osteoclasts (aOCs), mesenchymal stem cells (MSCs), precursor osteoblasts (pOBs), active osteoblasts (aOBs), and multiple myeloma cells. Additionally, we incorporate two signaling molecules including RANKL and bone derived factors (BDFs) such as transforming growth factor beta (TGF-β). In the sections below, we describe the interactions between cell types and cytokines that are key in bone remodeling and MM progression. Further details can be found in Supplementary Methods 1.

Parameters and grid

We implemented our model using the Hybrid Automata Library (HAL)[84]. When possible, parameters for the HCA model were derived from empirical and published data (Supplementary Tables 1-6). The model is defined on a 2D rectangular grid (160 x 150 pixels) representing a $1600 \times 1500\ \mu\mathrm{m}^2$ cross section of the bone marrow. Trabecular bone is defined in the center of the grid and initially consists of 12.9% of the total area, consistent with our *in vivo* data (Supplementary Methods 1.1). Normal bone remodeling events are uniformly distributed over 4 years, the approximate turnover time of trabecular bone[68]. A remodeling event is initiated by the expression of RANKL by five osteoblast lineage cells on the perimeter of the bone.

pOCs and osteoclasts

Precursor osteoclasts follow the gradient of RANKL to the bone remodeling site. With a given probability, at least five pOCs will fuse together to become a multinucleated osteoclast. Active aOCs resorb bone matrix, leading to the release of BDF. We assume that the amount of bone that aOCs resorb is proportional to their lifespan of approximately 14 days[68,85].

MSCs, pOBs, and osteoblasts

After an aOC fuses, an MSC is placed on the grid within a radius of $40\ \mu\mathrm{m}$ of the aOC, provided there is not already an MSC within the neighborhood. This requirement ensures that MSCs are located adjacent to sites of bone remodeling and can couple bone resorption with bone formation[86]. MSCs undergo asymmetrical division to create pOBs, which proliferate when BDF is above a certain threshold or differentiate into bone matrix-producing osteoblasts when BDF is below the threshold (Supplementary Fig. 2c). We assume that aOB lifespan is proportional to the amount of bone that was resorbed at the location of the aOB, which is approximately 3 months.

Cytokines

RANKL (R_L) and BDF (T_β) are two key cytokines that drive the normal bone remodeling process. RANKL is produced by osteoblast lineage cells ($\alpha_R B_{i,j}$) with natural decay of the ligand ($\delta_R R_L$). BDF is released during bone resorption ($\alpha_T B_{i,j} C_{i,j}$) with natural decay of the ligand ($\delta_T T_\beta$). We also assume that there is a constant production of BDFs (α_B) by other cell types that are not explicitly defined in the model. These cytokines are

incorporated into our model through the following system of partial differential equations (PDEs):

$$\frac{\partial R_L(x,y,t)}{\partial t} = \underbrace{D_R\left(\frac{\partial^2 R_L}{\partial x^2} + \frac{\partial^2 R_L}{\partial y^2}\right)}_{\text{Diffusion}} + \underbrace{\alpha_R B_{i,j}}_{\text{Production}} - \underbrace{\delta_R R_L}_{\text{Decay}}$$

$$\frac{\partial T_\beta(x,y,t)}{\partial t} = \underbrace{D_T\left(\frac{\partial^2 T_\beta}{\partial x^2} + \frac{\partial^2 T_\beta}{\partial y^2}\right)}_{\text{Diffusion}} + \underbrace{\alpha_B}_{\text{Basal Production}} + \underbrace{\alpha_T B_{i,j} C_{i,j}}_{\text{Production}} - \underbrace{\delta_T T_\beta}_{\text{Decay}}$$

where the subscripts specify the location on the grid, i.e. $x = ih$, $y = jh$ where $\{i, j\}$ are positive integers and h denotes the spatial step, $h = \Delta x = \Delta y$. The system of PDEs is solved using the forward time centered space (FTCS) scheme with periodic boundary conditions imposed on all sides of the domain, which is implemented using the diffusion function in HAL.

Multiple Myeloma

A single myeloma cell is recruited within a radius of $40\ \mu\text{m}$ of an aOC after the first aOC fusion event occurs (Fig. 4a). MM cells move and proliferate in response to BDF and have a further proliferative advantage if they are within a radius of $20\ \mu\text{m}$ of an MSC or pOB (Fig. 3g), and a survival advantage if BDF is above a certain threshold (Fig. 3h). As the MM cell population increases, additional MSCs are recruited. Furthermore, if three or more myeloma cells are located close to bone, a new bone remodeling event is initiated which increases RANKL and aOC formation. MM cells also prevent the differentiation of pOBs if they are located within a radius of $80\ \mu\text{m}$ of a MM cell which decreases aOB activity.

Treatment

The HCA incorporates the direct and indirect effects of bortezomib by including the cytotoxic effect on MM cells as well as its ability to inhibit pOC fusion and enhance bone formation[33,34] (Supplementary Fig. 3). To mimic the clinical scenario of MM diagnosis, once MM reaches 10% of the bone marrow area *in silico*, treatment is applied either continuously or pulsed (2 weeks on, 1 week off) until MM burden reaches 20% of the bone marrow. In these simulations, once treatment is initiated, myeloma cells have a probability of mutation during cell division that would cause the MM cells to become

resistant to bortezomib. MM cells that are within a radius of $20\ \mu m$ of an MSC or pOB or are located at a position where BDF is above a certain threshold, have a survival advantage during treatment referred to as environment mediated drug resistance (EMDR).

U266^{GFP} multiple myeloma mouse model

All animal experiments were performed with University of South Florida (Tampa, FL) Institutional Animal Care and Use Committee approval (CCL; #7356R). Male and female 14-16 week-old immunodeficient mice NOD-SCIDγ (NSG) mice were divided into tumor naïve or tumor bearing mice (25/group). GFP-expressing human U266 (U266-GFP) multiple myeloma cells were injected ($5x10^6$cells/100µL PBS) or PBS (100µL) via tail vein. Mice were euthanized at days 3, 10, 20, 40 and 100 (5/group/timepoint). Tibiae were excised and soft tissue removed for histological and FACs analyses.

Micro-computed Tomography, Immunofluorescence and Histomorphometry,

Harvested right tibiae were fixed in 4% paraformaldehyde (PFA) in 1x phosphate buffered saline (PBS) for 48 hours at room temperature. Evaluation of trabecular bone microarchitecture was performed in a region of 1000 µm, beginning 500 µm from the growth plate using the SCANCO µ35CT scanner. Tibiae were decalcified in an excess of 10% EDTA at pH 7.4 at 4°C for up to three weeks with changes every 3 days before being place in cryoprotection buffer (30% sucrose), frozen in cryomedium (OCT) and subjected to cryosectioning to yield 20 µm tissue sections. Sections were dried, washed and blocked before addition of primary antibodies (anti-pHH3; 06-570 Millipore, anti-Osterix; ab22552, abcam: anti-αSMA: PA5-16697, Invitrogen). Slides were washed and incubated with goat anti-rabbit Alexa Fluor-647-conjugated secondary antibody and counterstained with DAPI. Mounted sections were imaged using 10X image tile-scans of whole tibia. pHH3+, αSMA+, Osterix+ or GFP+ cells were identified and quantified using Fiji software[87]. Dual ALP and TRAcP staining were performed on cryosections. Brightfield visualization was performed using the EVOS auto at 20X magnification. Five images per section were taken and the number of ALP+ cuboidal bone-lining osteoblasts and red multinucleated TRAcP+ osteoclasts per bone surface were calculated.

For additional and in-depth methods, please see supplementary materials.

Author Contributions

A.K.M and D.B. were responsible for computational model design and execution. R.T.B and C.C.L were responsible for biological experimentation design, and analysis**.** T.L and N.N performed biological experiments**.** A.K.M, R.T.B, C.C.L and D.B were involved in overall concept and design. All authors were involved in data interpretation, manuscript writing and editing.

Acknowledgements

The authors would like to thank Jeremy Frieling, Mostafa Nasr, Marilena Tauro, Matthew Froid, Tatiana Miti, Malgorzata Tyczynska, Mark Robertson-Tessi, Etienne Baratchart, and Ariosto Siquiera Silva at Moffitt Cancer Center for insightful discussions over the years and with editing and revision of manuscript. This work has been supported in part by the Small Animal Imaging Laboratory (SAIL) and the Flow Cytometry, and Analytical Microscopy Core Facilities at the Moffitt Cancer Center, an NCI designated Comprehensive Cancer Center (P30-CA076292). This work was supported in part by funds from the NCI PSON (5U01CA244101).

References:

1. Howlader N, N.A., Krapcho M, Miller D, Brest A, Yu M, Ruhl J, Tatalovich Z, Mariotto A, Lewis DR, Chen HS, Feuer EJ, Cronin KA SEER Cancer Statistics Review, 1975-2016, National Cancer Institute. (2019).
2. Cowan, A.J.*, et al.* Diagnosis and Management of Multiple Myeloma: A Review. *JAMA* **327**, 464-477 (2022).
3. Azab, A.K.*, et al.* Hypoxia promotes dissemination of multiple myeloma through acquisition of epithelial to mesenchymal transition-like features. *Blood* **119**, 5782-5794 (2012).
4. Uchiyama, H., Barut, B.A., Mohrbacher, A.F., Chauhan, D. & Anderson, K.C. Adhesion of human myeloma-derived cell lines to bone marrow stromal cells stimulates interleukin-6 secretion. *Blood* **82**, 3712-3720 (1993).
5. Hao, M.*, et al.* Bone marrow stromal cells protect myeloma cells from bortezomib induced apoptosis by suppressing microRNA-15a expression. *Leuk Lymphoma* **52**, 1787-1794 (2011).
6. Markovina, S.*, et al.* Bone marrow stromal cells from multiple myeloma patients uniquely induce bortezomib resistant NF-kappaB activity in myeloma cells. *Mol Cancer* **9**, 176 (2010).
7. Roccaro, A.M.*, et al.* BM mesenchymal stromal cell-derived exosomes facilitate multiple myeloma progression. *J Clin Invest* **123**, 1542-1555 (2013).
8. Azab, A.K.*, et al.* CXCR4 inhibitor AMD3100 disrupts the interaction of multiple myeloma cells with the bone marrow microenvironment and enhances their sensitivity to therapy. *Blood* **113**, 4341-4351 (2009).
9. Meads, M.B., Gatenby, R.A. & Dalton, W.S. Environment-mediated drug resistance: a major contributor to minimal residual disease. *Nat Rev Cancer* **9**, 665-674 (2009).
10. Meads, M.B., Hazlehurst, L.A. & Dalton, W.S. The bone marrow microenvironment as a tumor sanctuary and contributor to drug resistance. *Clin Cancer Res* **14**, 2519-2526 (2008).
11. Di Marzo, L.*, et al.* Microenvironment drug resistance in multiple myeloma: emerging new players. *Oncotarget* **7**, 60698-60711 (2016).
12. Edwards, C.M., Zhuang, J. & Mundy, G.R. The pathogenesis of the bone disease of multiple myeloma. *Bone* **42**, 1007-1013 (2008).
13. Wuilleme-Toumi, S.*, et al.* Mcl-1 is overexpressed in multiple myeloma and associated with relapse and shorter survival. *Leukemia* **19**, 1248-1252 (2005).
14. Chen, S.*, et al.* A Bim-targeting strategy overcomes adaptive bortezomib resistance in myeloma through a novel link between autophagy and apoptosis. in *Blood*, Vol. 124 2687-2697 (2014).
15. Touzeau, C., Maciag, P., Amiot, M. & Moreau, P. Targeting Bcl-2 for the treatment of multiple myeloma. *Leukemia* **32**, 1899-1907 (2018).
16. Kumar, S.*, et al.* Efficacy of venetoclax as targeted therapy for relapsed/refractory t(11;14) multiple myeloma. *Blood* **130**, 2401-2409 (2017).
17. Pasetto, S., Enderling, H., Gatenby, R.A. & Brady-Nicholls, R. Intermittent Hormone Therapy Models Analysis and Bayesian Model Comparison for Prostate Cancer. *Bull Math Biol* **84**, 2 (2021).

18. Brady-Nicholls, R.*, et al.* Predicting patient-specific response to adaptive therapy in metastatic castration-resistant prostate cancer using prostate-specific antigen dynamics. *Neoplasia* **23**, 851-858 (2021).
19. West, J.B.*, et al.* Multidrug Cancer Therapy in Metastatic Castrate-Resistant Prostate Cancer: An Evolution-Based Strategy. *Clin Cancer Res* **25**, 4413-4421 (2019).
20. Araujo, A.*, et al.* Quantification and Optimization of Standard-of-Care Therapy to Delay the Emergence of Resistant Bone Metastatic Prostate Cancer. *Cancers (Basel)* **13**(2021).
21. Gallaher, J.*, et al.* Improving treatment strategies for patients with metastatic castrate resistant prostate cancer through personalized computational modeling. *Clin Exp Metastasis* **31**, 991-999 (2014).
22. Macklin, P., Edgerton, M.E., Thompson, A.M. & Cristini, V. Patient-calibrated agent-based modelling of ductal carcinoma in situ (DCIS): from microscopic measurements to macroscopic predictions of clinical progression. *J Theor Biol* **301**, 122-140 (2012).
23. Gallaher, J.A.*, et al.* From cells to tissue: How cell scale heterogeneity impacts glioblastoma growth and treatment response. *PLoS Comput Biol* **16**, e1007672 (2020).
24. Alfonso, J.C.L.*, et al.* Tumor-immune ecosystem dynamics define an individual Radiation Immune Score to predict pan-cancer radiocurability. *Neoplasia* **23**, 1110-1122 (2021).
25. Jilka, R.L. Biology of the basic multicellular unit and the pathophysiology of osteoporosis. *Med Pediatr Oncol* **41**, 182-185 (2003).
26. Wang, L., You, X., Zhang, L., Zhang, C. & Zou, W. Mechanical regulation of bone remodeling. *Bone Res* **10**, 16 (2022).
27. Janssens, K., ten Dijke, P., Janssens, S. & Van Hul, W. Transforming growth factor-beta1 to the bone. *Endocr Rev* **26**, 743-774 (2005).
28. Sims, N.A. & Martin, T.J. Osteoclasts Provide Coupling Signals to Osteoblast Lineage Cells Through Multiple Mechanisms. *Annu Rev Physiol* **82**, 507-529 (2020).
29. Edwards, J.R.*, et al.* Inhibition of TGF-beta signaling by 1D11 antibody treatment increases bone mass and quality in vivo. *J Bone Miner Res* **25**, 2419-2426 (2010).
30. Paton-Hough, J.*, et al.* Preventing and Repairing Myeloma Bone Disease by Combining Conventional Antiresorptive Treatment With a Bone Anabolic Agent in Murine Models. *J Bone Miner Res* **34**, 783-796 (2019).
31. Pan, B.*, et al.* The nitrogen-containing bisphosphonate, zoledronic acid, increases mineralisation of human bone-derived cells in vitro. *Bone* **34**, 112-123 (2004).
32. Zangari, M., Yaccoby, S., Cavallo, F., Esseltine, D. & Tricot, G. Response to bortezomib and activation of osteoblasts in multiple myeloma. *Clin Lymphoma Myeloma* **7**, 109-114 (2006).
33. Pennisi, A.*, et al.* The proteasome inhibitor, bortezomib suppresses primary myeloma and stimulates bone formation in myelomatous and nonmyelomatous bones in vivo. *Am J Hematol* **84**, 6-14 (2009).

34. Hurchla, M.A., *et al.* The epoxyketone-based proteasome inhibitors carfilzomib and orally bioavailable oprozomib have anti-resorptive and bone-anabolic activity in addition to anti-myeloma effects. *Leukemia* **27**, 430-440 (2013).
35. Galson, D.L., Silbermann, R. & Roodman, G.D. Mechanisms of multiple myeloma bone disease. *Bonekey Rep* **1**, 135 (2012).
36. Hewett, D.R., *et al.* DNA Barcoding Reveals Habitual Clonal Dominance of Myeloma Plasma Cells in the Bone Marrow Microenvironment. *Neoplasia* **19**, 972-981 (2017).
37. Lawson, M.A., *et al.* Osteoclasts control reactivation of dormant myeloma cells by remodelling the endosteal niche. *Nat Commun* **6**(2015).
38. Jones, E.A., *et al.* Optimization of a flow cytometry-based protocol for detection and phenotypic characterization of multipotent mesenchymal stromal cells from human bone marrow. *Cytometry B Clin Cytom* **70**, 391-399 (2006).
39. Noll, J.E., *et al.* Myeloma plasma cells alter the bone marrow microenvironment by stimulating the proliferation of mesenchymal stromal cells. *Haematologica* **99**, 163-171 (2014).
40. Marino, S., Petrusca, D.N. & Roodman, G.D. Therapeutic targets in myeloma bone disease. *Br J Pharmacol* **178**, 1907-1922 (2021).
41. Kassen, D., *et al.* Myeloma impairs mature osteoblast function but causes early expansion of osteo-progenitors: temporal changes in bone physiology and gene expression in the KMS12BM model. *Br J Haematol* **172**, 64-79 (2016).
42. LeBlanc, R., *et al.* Proteasome inhibitor PS-341 inhibits human myeloma cell growth in vivo and prolongs survival in a murine model. *Cancer Res* **62**, 4996-5000 (2002).
43. Manasanch, E.E. & Orlowski, R.Z. Proteasome inhibitors in cancer therapy. *Nat Rev Clin Oncol* **14**, 417-433 (2017).
44. Morgan, G.J., *et al.* First-line treatment with zoledronic acid as compared with clodronic acid in multiple myeloma (MRC Myeloma IX): a randomised controlled trial. *Lancet* **376**, 1989-1999 (2010).
45. Accardi, F., *et al.* Mechanism of Action of Bortezomib and the New Proteasome Inhibitors on Myeloma Cells and the Bone Microenvironment: Impact on Myeloma-Induced Alterations of Bone Remodeling. *Biomed Res Int* **2015**, 172458 (2015).
46. Gatenby, R.A., Silva, A.S., Gillies, R.J. & Frieden, B.R. Adaptive therapy. *Cancer Res* **69**, 4894-4903 (2009).
47. Keats, J.J., *et al.* Clonal competition with alternating dominance in multiple myeloma. *Blood* **120**, 1067-1076 (2012).
48. Paino, T., *et al.* Phenotypic identification of subclones in multiple myeloma with different chemoresistant, cytogenetic and clonogenic potential. *Leukemia* **29**, 1186-1194 (2015).
49. Walker, B.A., *et al.* Intraclonal heterogeneity is a critical early event in the development of myeloma and precedes the development of clinical symptoms. *Leukemia* **28**, 384-390 (2014).
50. Paiva, B., *et al.* Phenotypic and genomic analysis of multiple myeloma minimal residual disease tumor cells: a new model to understand chemoresistance. *Blood* **127**, 1896-1906 (2016).

51. Ayati, B.P., Edwards, C.M., Webb, G.F. & Wikswo, J.P. A mathematical model of bone remodeling dynamics for normal bone cell populations and myeloma bone disease. *Biol Direct* **5**, 28 (2010).
52. Ji, B., Genever, P.G. & Fagan, M.J. A virtual approach to evaluate therapies for management of multiple myeloma induced bone disease. *Int J Numer Method Biomed Eng* **32**, e02735 (2016).
53. Ji, B., Genever, P.G., Patton, R.J. & Fagan, M.J. Mathematical modelling of the pathogenesis of multiple myeloma-induced bone disease. *Int J Numer Method Biomed Eng* **30**, 1085-1102 (2014).
54. Sartakhti, J.S., Manshaei, M.H., Bateni, S. & Archetti, M. Evolutionary Dynamics of Tumor-Stroma Interactions in Multiple Myeloma. *PLoS One* **11**, e0168856 (2016).
55. Wang, Y., Pivonka, P., Buenzli, P.R., Smith, D.W. & Dunstan, C.R. Computational modeling of interactions between multiple myeloma and the bone microenvironment. *PLoS One* **6**, e27494 (2011).
56. Qiao, M., Wu, D., Carey, M., Zhou, X. & Zhang, L. Multi-Scale Agent-Based Multiple Myeloma Cancer Modeling and the Related Study of the Balance between Osteoclasts and Osteoblasts. *PLoS One* **10**, e0143206 (2015).
57. Dingli, D., Chalub, F.A., Santos, F.C., Van Segbroeck, S. & Pacheco, J.M. Cancer phenotype as the outcome of an evolutionary game between normal and malignant cells. *Br J Cancer* **101**, 1130-1136 (2009).
58. Picco, N., Sahai, E., Maini, P.K. & Anderson, A.R.A. Integrating Models to Quantify Environment-Mediated Drug Resistance. *Cancer Res* **77**, 5409-5418 (2017).
59. Su, J.*, et al.* Targeting the biophysical properties of the myeloma initiating cell niches: a pharmaceutical synergism analysis using multi-scale agent-based modeling. *PLoS One* **9**, e85059 (2014).
60. Perez-Velazquez, J., Gevertz, J.L., Karolak, A. & Rejniak, K.A. Microenvironmental Niches and Sanctuaries: A Route to Acquired Resistance. *Adv Exp Med Biol* **936**, 149-164 (2016).
61. Perez-Velazquez, J. & Rejniak, K.A. Drug-Induced Resistance in Micrometastases: Analysis of Spatio-Temporal Cell Lineages. *Front Physiol* **11**, 319 (2020).
62. Ghobrial, I.M.*, et al.* A Phase Ib/II Trial of the First-in-Class Anti-CXCR4 Antibody Ulocuplumab in Combination with Lenalidomide or Bortezomib Plus Dexamethasone in Relapsed Multiple Myeloma. *Clin Cancer Res* **26**, 344-353 (2020).
63. Ghobrial, I.M.*, et al.* Phase I/II trial of the CXCR4 inhibitor plerixafor in combination with bortezomib as a chemosensitization strategy in relapsed/refractory multiple myeloma. *Am J Hematol* **94**, 1244-1253 (2019).
64. Suzuki, K., Nishiwaki, K. & Yano, S. Treatment Strategies Considering Micro-Environment and Clonal Evolution in Multiple Myeloma. *Cancers (Basel)* **13**(2021).
65. Zhang, J., Cunningham, J., Brown, J. & Gatenby, R. Evolution-based mathematical models significantly prolong response to abiraterone in metastatic castrate-resistant prostate cancer and identify strategies to further improve outcomes. *Elife* **11**(2022).

66. Frankenstein, Z.*, et al.* Stromal reactivity differentially drives tumour cell evolution and prostate cancer progression. *Nat Ecol Evol* **4**, 870-884 (2020).
67. Jenner, A.L.*, et al.* Agent-based computational modeling of glioblastoma predicts that stromal density is central to oncolytic virus efficacy. *iScience* **25**, 104395 (2022).
68. Manolagas, S.C. Birth and death of bone cells: basic regulatory mechanisms and implications for the pathogenesis and treatment of osteoporosis. *Endocr Rev* **21**, 115-137 (2000).
69. Lemaire, V., Tobin, F.L., Greller, L.D., Cho, C.R. & Suva, L.J. Modeling the interactions between osteoblast and osteoclast activities in bone remodeling. *J Theor Biol* **229**, 293-309 (2004).
70. Schenck, R.O.*, et al.* Gattaca: Base-Pair Resolution Mutation Tracking for Somatic Evolution Studies using Agent-based Models. *Mol Biol Evol* **39**(2022).
71. West, J., Schenck, R.O., Gatenbee, C., Robertson-Tessi, M. & Anderson, A.R.A. Normal tissue architecture determines the evolutionary course of cancer. *Nat Commun* **12**, 2060 (2021).
72. Shay, G., Hazlehurst, L. & Lynch, C.C. Dissecting the multiple myeloma-bone microenvironment reveals new therapeutic opportunities. *J Mol Med (Berl)* **94**, 21-35 (2016).
73. Moser-Katz, T., Joseph, N.S., Dhodapkar, M.V., Lee, K.P. & Boise, L.H. Game of Bones: How Myeloma Manipulates Its Microenvironment. *Front Oncol* **10**, 625199 (2020).
74. Kawano, Y.*, et al.* Targeting the bone marrow microenvironment in multiple myeloma. *Immunol Rev* **263**, 160-172 (2015).
75. Zavidij, O.*, et al.* Single-cell RNA sequencing reveals compromised immune microenvironment in precursor stages of multiple myeloma. *Nat Cancer* **1**, 493-506 (2020).
76. Gallaher, J.A., Enriquez-Navas, P.M., Luddy, K.A., Gatenby, R.A. & Anderson, A.R.A. Spatial Heterogeneity and Evolutionary Dynamics Modulate Time to Recurrence in Continuous and Adaptive Cancer Therapies. *Cancer Res* **78**, 2127-2139 (2018).
77. Gallaher, J.*, et al.* Methods for determining key components in a mathematical model for tumor-immune dynamics in multiple myeloma. *J Theor Biol* **458**, 31-46 (2018).
78. Vander Velde, R.*, et al.* Resistance to targeted therapies as a multifactorial, gradual adaptation to inhibitor specific selective pressures. *Nat Commun* **11**, 2393 (2020).
79. Anderson, A.R., Weaver, A.M., Cummings, P.T. & Quaranta, V. Tumor morphology and phenotypic evolution driven by selective pressure from the microenvironment. *Cell* **127**, 905-915 (2006).
80. Araujo, A., Cook, L.M., Lynch, C.C. & Basanta, D. Size Matters: Metastatic cluster size and stromal recruitment in the establishment of successful prostate cancer to bone metastases. *Bull Math Biol* **80**, 1046-1058 (2018).
81. Cook, L.M.*, et al.* Predictive computational modeling to define effective treatment strategies for bone metastatic prostate cancer. *Sci Rep* **6**, 29384 (2016).

82. Araujo, A., Cook, L.M., Lynch, C.C. & Basanta, D. An integrated computational model of the bone microenvironment in bone-metastatic prostate cancer. *Cancer Res* **74**, 2391-2401 (2014).
83. Anderson, A.R. A hybrid mathematical model of solid tumour invasion: the importance of cell adhesion. *Math Med Biol* **22**, 163-186 (2005).
84. Bravo, R.R.*, et al.* Hybrid Automata Library: A flexible platform for hybrid modeling with real-time visualization. *PLoS Comput Biol* **16**, e1007635 (2020).
85. Jilka, R.L., Weinstein, R.S., Bellido, T., Parfitt, A.M. & Manolagas, S.C. Osteoblast programmed cell death (apoptosis): modulation by growth factors and cytokines. *J Bone Miner Res* **13**, 793-802 (1998).
86. Tang, Y.*, et al.* TGF-beta1-induced migration of bone mesenchymal stem cells couples bone resorption with formation. *Nat Med* **15**, 757-765 (2009).
87. Schindelin, J.*, et al.* Fiji: an open-source platform for biological-image analysis. *Nat Methods* **9**, 676-682 (2012).
88. Gatenbee, C.D., Schenck, R.O., Bravo, R.R. & Anderson, A.R.A. EvoFreq: visualization of the Evolutionary Frequencies of sequence and model data. *BMC Bioinformatics* **20**, 710 (2019).

Figure Legends

Fig. 1. Development of a hybrid HCA of the naïve and myeloma bone microenvironment. a, Bone-lining osteoblast lineage cells release RANKL inducing fusion and maturation of osteoclasts (1). Osteoclasts resorb the bone, releasing stored bone-derived factors (BDFs) such as TGF-β (2). TGF-β recruits local MSCs and stimulates asymmetric division in to preosteoblasts (2). When TGF-β levels remain high, pOBs rapidly proliferate. Following osteoclast apoptosis, release of TGF-β falls and pOBs differentiate to mature bone producing osteoblasts (3). While TGF-β levels remain low, osteoblasts produce new bone (4). As bone returns to normal, a fraction of the osteoblasts are buried within the matrix becoming terminally differentiated osteoblasts (5), the remaining OBs undergo apoptosis, or become quiescent bone-lining cells (6). Myeloma cells enhance the formation of osteoclasts (7), enhanced bone resorption produces higher levels of BDFs which fuel myeloma growth (8) and inhibit osteoblast differentiation (8) and activity (9). **b**, Interaction diagram between cell types in the HCA and factors such as BDFs and RANKL. **c**, Flowcharts describing the sequence of steps followed by pOCs, aOCs, MSCs, pOBs, aOBs, and myeloma cells.

Fig. 2. The HCA model captures all stages of bone homeostasis.
a, Images from simulations at initial conditions (left) and after 4 years (right). Legend depicts colors of cell types in the model. **b**, BMU is initiated in response to release of RANKL from bone lining cells (1). pOCs migrate to RANKL and fuse to form an aOC under highest concentrations (2). aOC resorbs bone and stored BDFs are released which recruits MSCs. MSCs divide asymmetrically producing pOBs which proliferate rapidly under high TGF-β conditions. Upon completion of resorption, BDF levels fall allowing for pOB differentiation to aOBs. aOBs form new bone (4) and ultimately undergo apoptosis or become quiescent bone lining cells (5).

Fig. 3. Multiple myeloma cells receive proliferative and survival advantages from the bone marrow microenvironment. a, Quantification of the distance of phosphorylated histone H3 positive (pHH3+; red) myeloma cells (green) to the nearest

trabecular or cortical bone in U266^{GFP}-bearing mice 100 days post inoculation. **b,** Representative images from experiment in **a**, DAPI (blue) was used as a nuclear counterstain. White dotted line indicates tumor bone interface. Scale bar, 50 microns. **c,** Quantification of the distance of TUNEL+ (red) myeloma cells (green) to the nearest trabecular or cortical bone in U266^{GFP}-bearing mice 100 days post inoculation. **d,** Representative image from experiment described in **c**, DAPI (blue) was used as a nuclear counterstain. White dotted line indicates tumor bone interface. Scale bar, 50 microns. **e,** Images of huMSCs differentiated to different stages of the osteoblast lineage. Cells were stained with Alizarin Red to identify mineralization. **f,** Proliferation index of CM-DiL stained U266 cells 7 days after growth in 50% conditioned medium from control wells or cells of the OB lineage. Results are displayed as means of at least 3 experiments. **g,** Plot of functional form used to represent the division rate of myeloma cells in the presence and absence of pOBs/MSCs. **h,** Plot of functional form used to represent the death of myeloma cells when BDF is above and below a threshold.
* p-value < 0.05, ** p-value <0.01

Fig. 4. Computational and biological model outputs of myeloma growth and bone dynamics. a, HCA model images showing single myeloma cell (Day 5), colonization of the marrow by MM cells (Day 75), increased osteoclastogenesis (Day 75, RANKL), bone resorption (Day 75; BDF) and eventual takeover of the marrow by MM cells (Day 350). Light green myeloma cells indicate MM cells with proliferative or survival advantage. **b**, Myeloma growth dynamics in HCA model in the absence of treatment. **c**, Myeloma induced loss of trabecular bone in HCA model compared to normal bone homeostasis. **d**, Bone loss decreases rapidly with myeloma expansion *in silico*. **e**, Myeloma growth in bone marrow of mice inoculated with U266-GFP cells over time. **f**, Trabecular bone volume fraction (BV/TV) was assessed *ex vivo* with high-resolution microCT. **g**, Biological model shows rapid myeloma-induced bone loss.

Fig. 5. Computational and biological model outputs of cell types in the myeloma bone microenvironment. a-d, Computational model outputs of increasing MSC percentage of the marrow area (%MA) (**a**), loss of aOBs (**b**) rise and fall of pOB

percentage (**c**), and increasing aOC percentage due to growth of MM (**d**). **e-h**, *Ex vivo* analysis of histological sections from the U266-GFP myeloma model demonstrates increasing presence of αSMA+ MSCs (**e**), loss of ALP+ cuboidal osteoblasts (**f**), early increase and subsequent reduction of OSX+ pOBs (**g**) and increasing numbers of TRAcP+ multinucleated aOCs (**h**) compared to tumor naïve mice.

Fig. 6. EMDR contributes to minimal residual disease and relapse. a, GFP+ U266 MM were plated alone or with huMSCs in the presence or absence of BTZ; MM burden was measured after 72h by area covered by GFP+ cells. **b**, Interaction diagram showing the cell types and factors in the HCA that are affected by BTZ or contribute to EMDR. **c**, *In vivo* growth of MM cells with and without BTZ treatment, data was taken from [42]. **d-f,** Model outputs of MM growth with continuous BTZ treatment, +/- EMDR when MM cells do not mutate (**d**) or with a probability to mutate (10^{-4}, **e** or 10^{-3}, **f**) and develop resistance. **g-h**, Kaplan-Meier plot of relapse-free survival from simulations described in **e** and **f** (n = 125 simulations, **g** or n = 25 simulations, **h**).

Fig. 7. EMDR contributes to tumor heterogeneity upon relapse. a, HCA images from simulations with continuous BTZ application, with no mutational probability ($p_{mut} = 0$) or high mutational probability ($p_{mut} = 10^{-3}$) in the presence or absence of EMDR. **b**, Computational outputs of the proportion of BTZ-sensitive and BTZ-resistant MM cells at end-point of with $p_{mut} = 10^{-3}$. **c**, mean number of resistant sub-clones arising following BTZ treatment in tumors that reached 20% and with resistant subclones and the locations within the bone marrow microenvironment where each subclone originated, with/without EMDR from simulations described in **a**. n = 13/25 (No Treatment), n = 10/25 (No EMDR), n = 24/25 (EMDR). **d**, Muller plots of sensitive and individual BTZ resistant sub-clones from simulations described in **a-c**, created using EvoFreq[88]. Red arrows indicate start of BTZ treatment. **** p-value < 0.0001

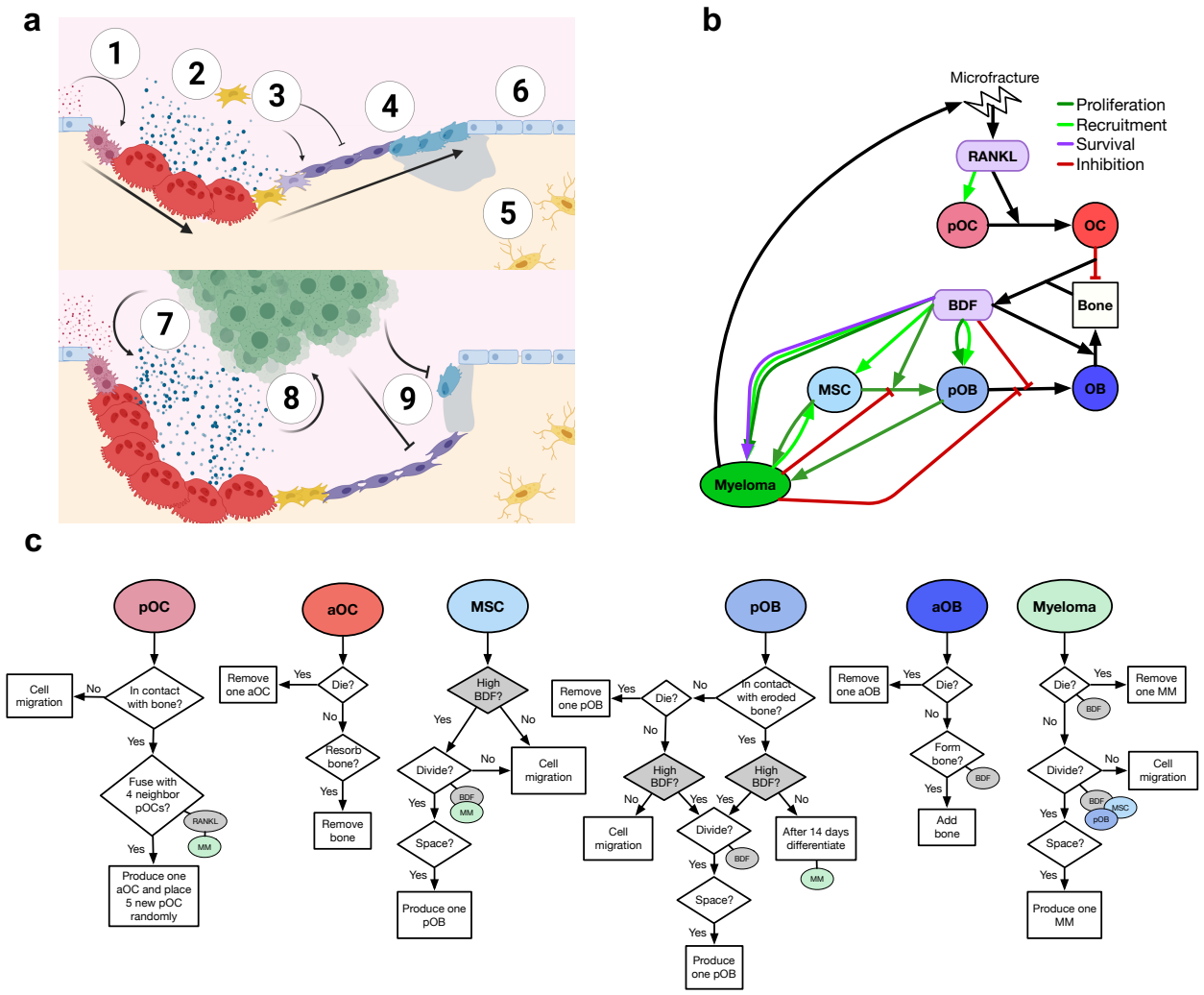
a
1
2
3
4
5
6
7
8
9
b
Microfracture
Proliferation
Recruitment
Survival
Inhibition
RANKL
pOC
OC
BDF
Bone
MSC
pOB
OB
Myeloma
c
pOC
Cell migration
No
In contact with bone?
Yes
Fuse with 4 neighbor pOCs?
RANKL
MM
Yes
Produce one aOC and place 5 new pOC randomly
aOC
Remove one aOC
Yes
Die?
No
Resorb bone?
Yes
Remove bone
MSC
High BDF?
Yes
No
Divide?
No
Cell migration
Yes
BDF
MM
Space?
Yes
Produce one pOB
pOB
Remove one pOB
Yes
Die?
No
In contact with eroded bone?
No
Yes
High BDF?
No
Cell migration
Yes
Divide?
Yes
BDF
Space?
Yes
Produce one pOB
High BDF?
No
After 14 days differentiate
MM
aOB
Remove one aOB
Yes
Die?
No
Form bone?
BDF
Yes
Add bone
Myeloma
Die?
Yes
Remove one MM
BDF
No
Divide?
No
Cell migration
Yes
BDF
MSC
pOB
Space?
Yes
Produce one MM

Fig. 1

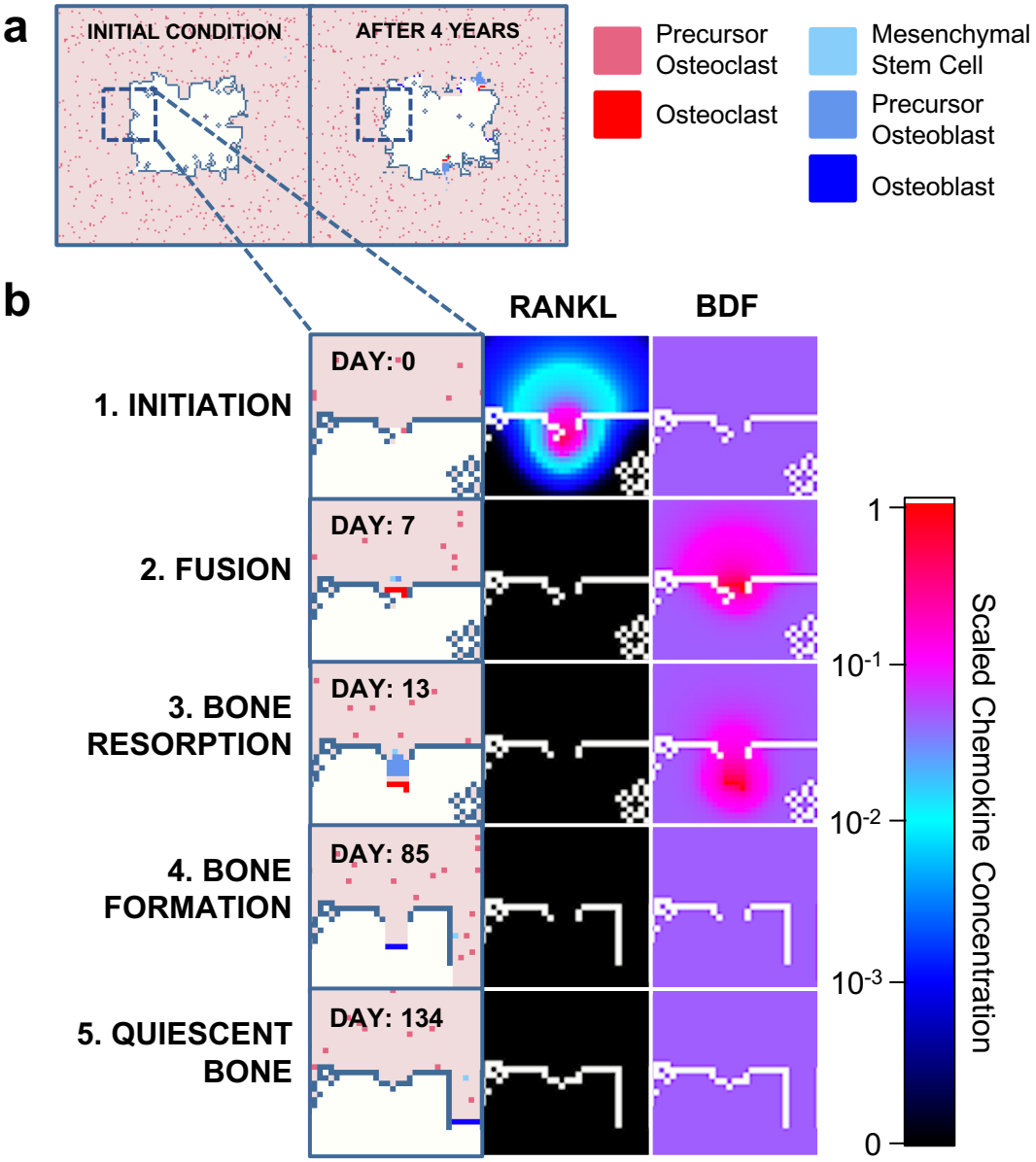
a
INITIAL CONDITION
AFTER 4 YEARS
Precursor Osteoclast
Osteoclast
Mesenchymal Stem Cell
Precursor Osteoblast
Osteoblast
b
RANKL
BDF
1. INITIATION
DAY: 0
2. FUSION
DAY: 7
3. BONE RESORPTION
DAY: 13
4. BONE FORMATION
DAY: 85
5. QUIESCENT BONE
DAY: 134
1
10-1
10-2
10-3
0
Scaled Chemokine Concentration

Fig. 2

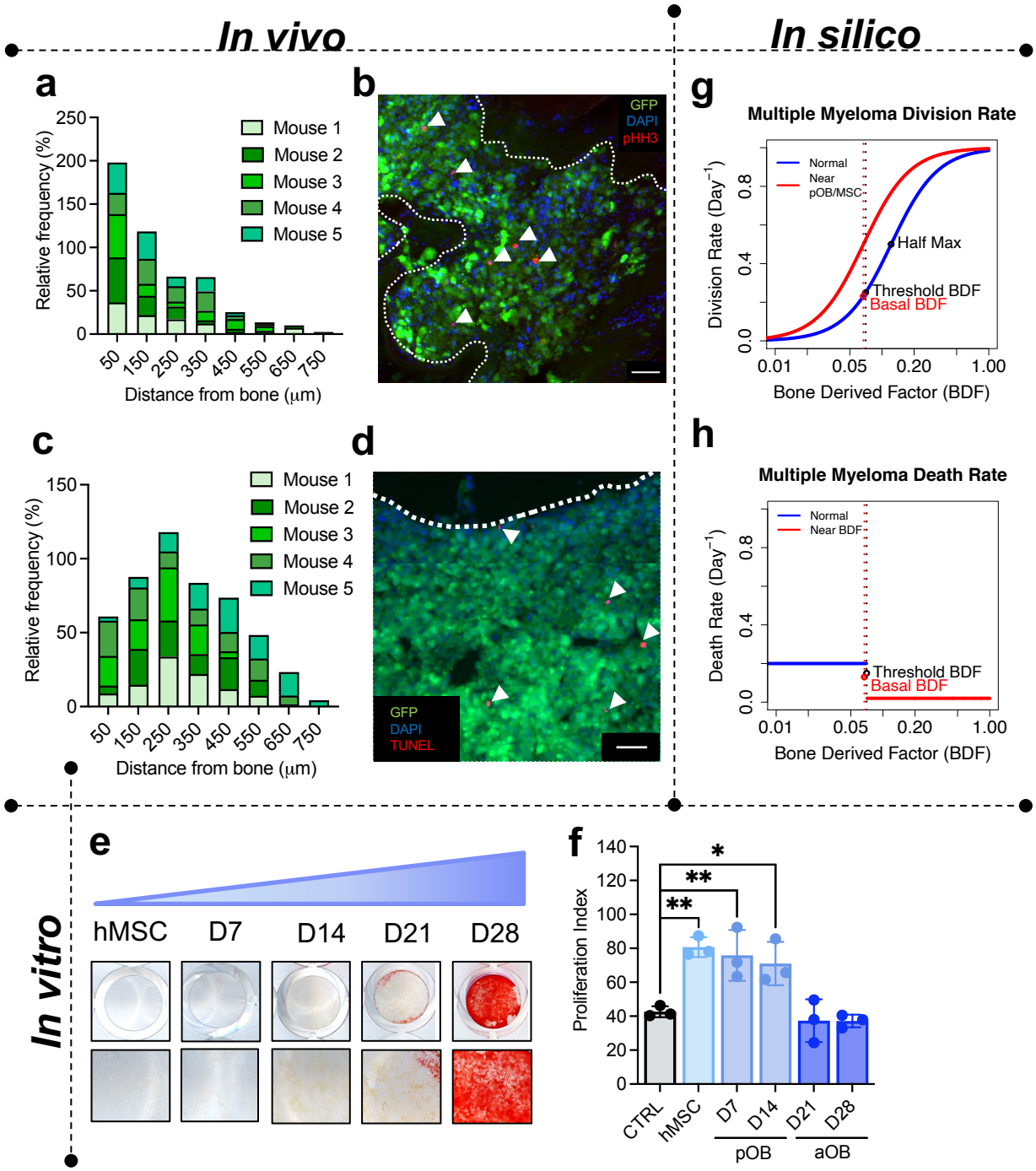
In vivo
In silico
a
Relative frequency (%)
Mouse 1
Mouse 2
Mouse 3
Mouse 4
Mouse 5
Distance from bone (μm)
b
GFP
DAPI
pHH3
c
Relative frequency (%)
Distance from bone (μm)
d
GFP
DAPI
TUNEL
g
Multiple Myeloma Division Rate
Division Rate (Day⁻¹)
Normal
Near pOB/MSC
Half Max
Threshold BDF
Basal BDF
Bone Derived Factor (BDF)
h
Multiple Myeloma Death Rate
Death Rate (Day⁻¹)
Normal
Near BDF
Threshold BDF
Basal BDF
Bone Derived Factor (BDF)
In vitro
e
hMSC
D7
D14
D21
D28
f
Proliferation Index
CTRL
hMSC
D7
D14
D21
D28
pOB
aOB

Fig. 3

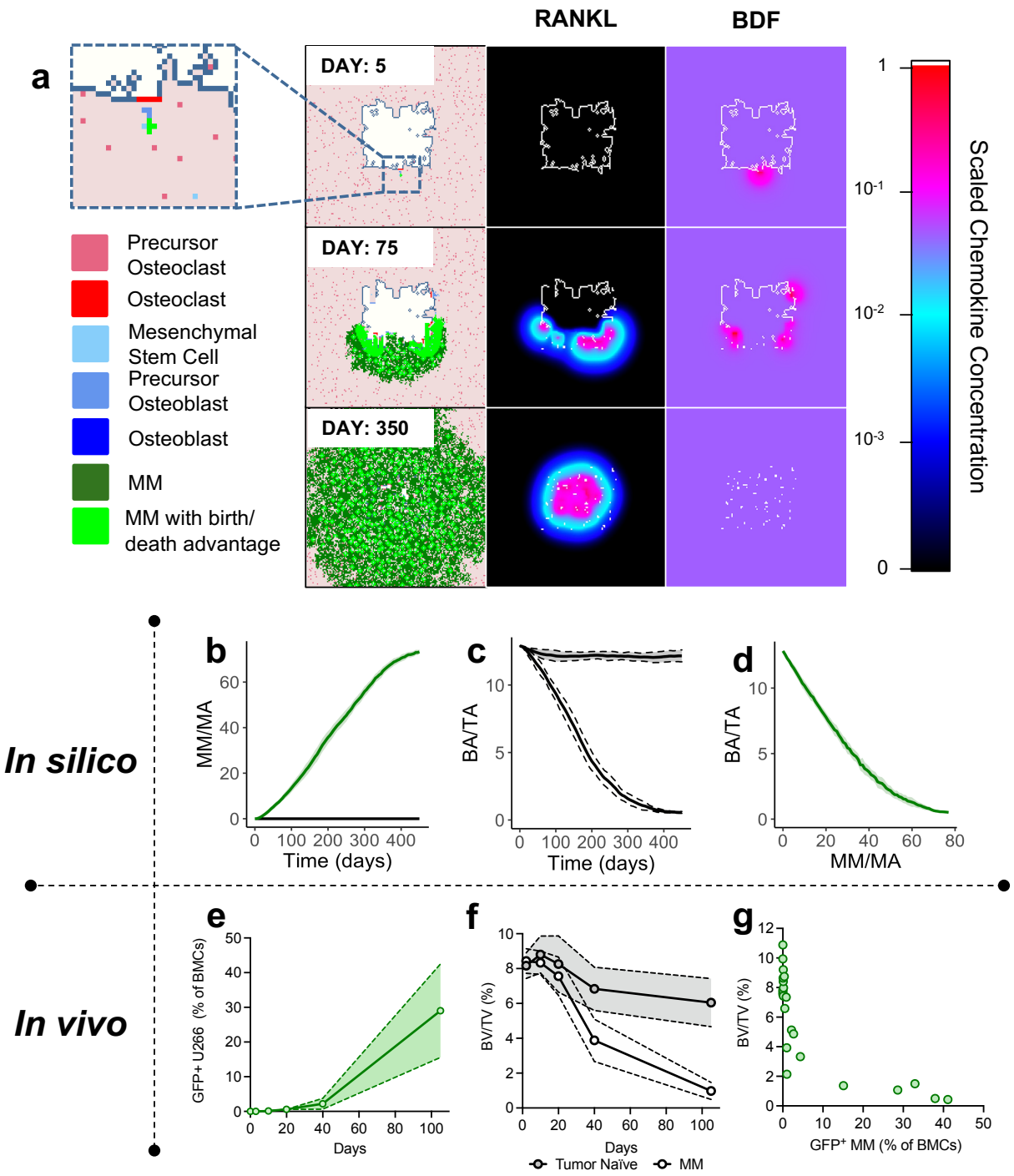
a
RANKL
BDF
DAY: 5
DAY: 75
DAY: 350
Precursor Osteoclast
Osteoclast
Mesenchymal Stem Cell
Precursor Osteoblast
Osteoblast
MM
MM with birth/ death advantage
Scaled Chemokine Concentration
1
10-1
10-2
10-3
0
In silico
In vivo
b
MM/MA
Time (days)
c
BA/TA
Time (days)
d
BA/TA
MM/MA
e
GFP+ U266 (% of BMCs)
Days
f
BV/TV (%)
Days
Tumor Naïve
MM
g
BV/TV (%)
GFP+ MM (% of BMCs)

Fig. 4

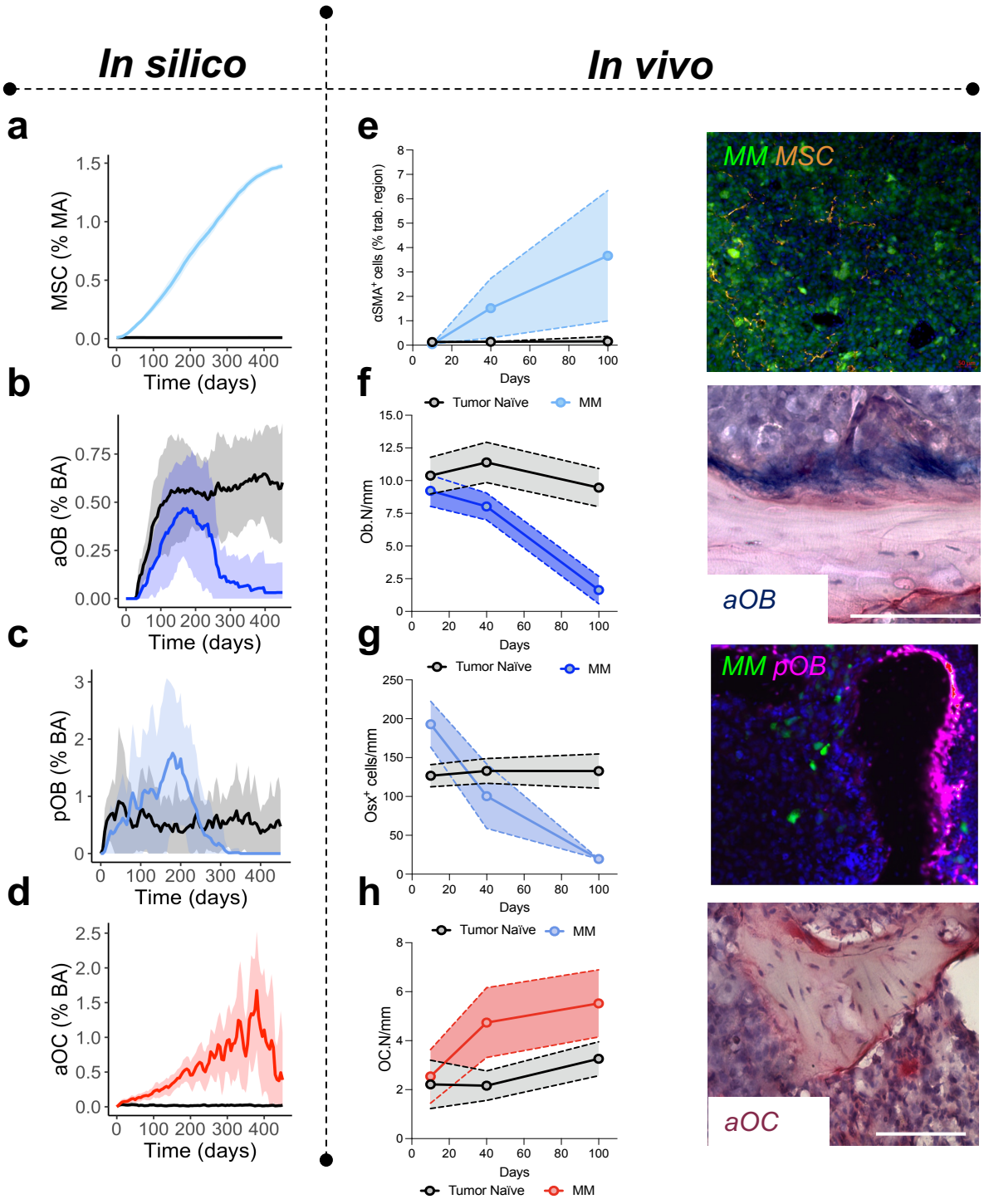
In silico
In vivo
a
MSC (% MA)
Time (days)
b
aOB (% BA)
Time (days)
c
pOB (% BA)
Time (days)
d
aOC (% BA)
Time (days)
e
αSMA+ cells (% trab. region)
Days
f
Ob.N/mm
Days
Tumor Naïve
MM
g
Osx+ cells/mm
Days
Tumor Naïve
MM
h
OC.N/mm
Days
Tumor Naïve
MM
MM MSC
aOB
MM pOB
aOC

Fig. 5

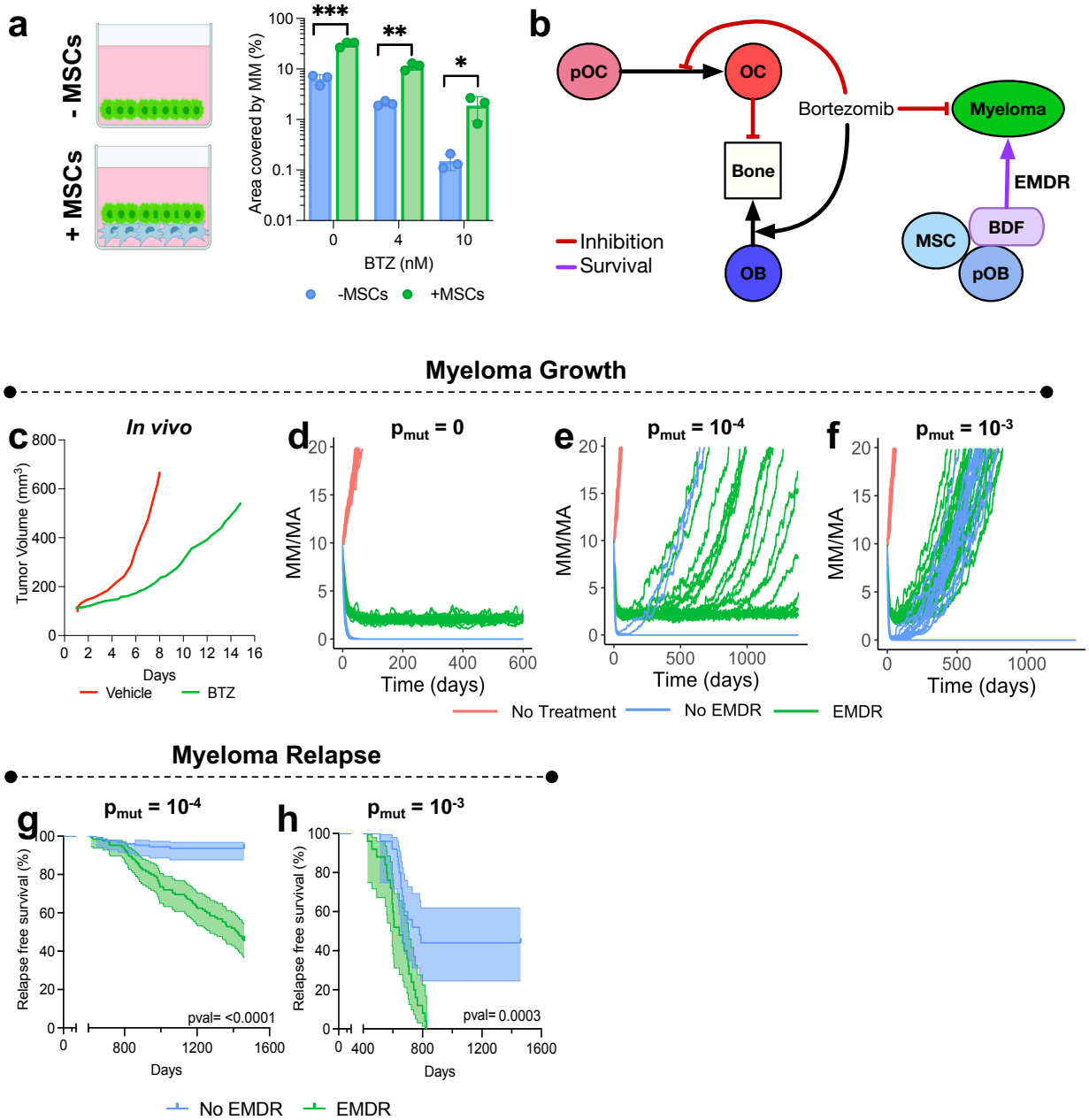
a
- MSCs
+ MSCs
Area covered by MM (%)
BTZ (nM)
-MSCs
+MSCs
b
pOC
OC
Bortezomib
Myeloma
Bone
EMDR
MSC
BDF
pOB
OB
Inhibition
Survival
Myeloma Growth
c
In vivo
Tumor Volume (mm³)
Days
Vehicle
BTZ
d
p_{mut} = 0
MM/MA
Time (days)
e
p_{mut} = 10^{-4}
f
p_{mut} = 10^{-3}
No Treatment
No EMDR
EMDR
Myeloma Relapse
g
p_{mut} = 10^{-4}
Relapse free survival (%)
pval= <0.0001
Days
h
p_{mut} = 10^{-3}
pval= 0.0003
No EMDR
EMDR

Fig. 6

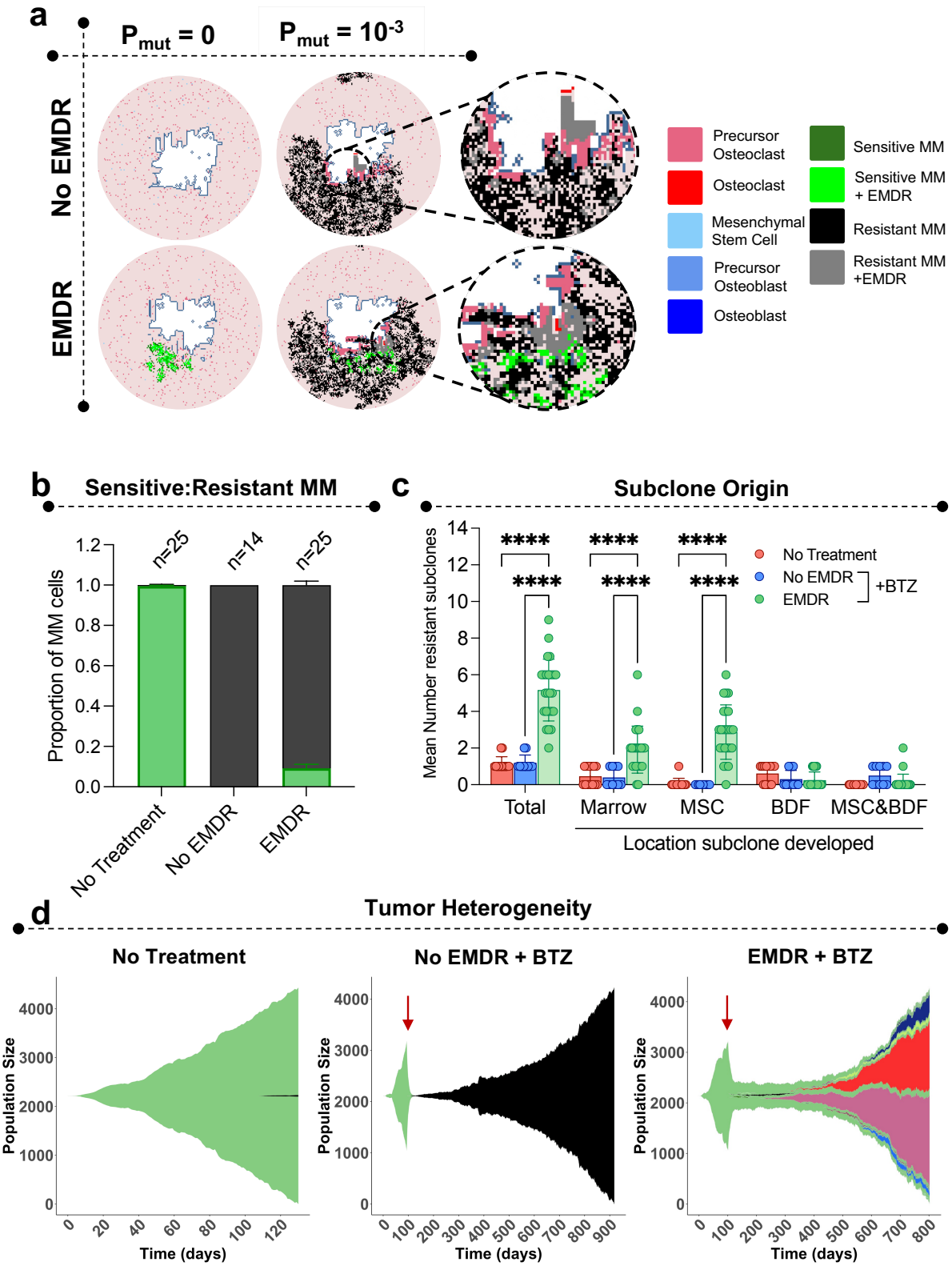
a
P_{mut} = 0
P_{mut} = 10^{-3}
No EMDR
EMDR
Precursor Osteoclast
Osteoclast
Mesenchymal Stem Cell
Precursor Osteoblast
Osteoblast
Sensitive MM
Sensitive MM + EMDR
Resistant MM
Resistant MM +EMDR
b
Sensitive:Resistant MM
Proportion of MM cells
n=25
n=14
n=25
No Treatment
No EMDR
EMDR
c
Subclone Origin
Mean Number resistant subclones
****
No Treatment
No EMDR
EMDR
+BTZ
Total
Marrow
MSC
BDF
MSC&BDF
Location subclone developed
d
Tumor Heterogeneity
No Treatment
No EMDR + BTZ
EMDR + BTZ
Population Size
Time (days)

Fig. 7